9170 *Macromolecules* **2009**, *42*, 9170–9182
DOI: 10.1021/ma901348j

Macromolecules
ARTICLE

Experimental and Numerical Studies of Tethered DNA Shear Dynamics in the Flow-Gradient Plane

Christopher A. Lueth[†] and Eric S. G. Shaqfeh*[,†,‡]

[†]*Department of Chemical Engineering, Stanford University, Stanford, California 94305, and* [‡]*Department of Mechanical Engineering, Stanford University, Stanford, California 94305*

Received June 23, 2009; Revised Manuscript Received October 5, 2009

ABSTRACT: We use a combination of theoretical predictions and λ-phage DNA single molecule fluorescence microscopy to study the behavior of polymers tethered to surfaces. Brownian dynamics simulations of a number of coarse-grained polymer models—dynamic and equilibrium Kratky−Porod chains as well as bead−spring chains—were completed and compared with analytical and experimental results. Experiments of tethered λ-phage DNA in shear flow are presented for the first time in the flow-gradient plane. Cyclic dynamics—where the polymer continuously diffuses away from the wall, subsequently undergoes stretch in the flow direction, is then "entropically pulled back" toward the wall, and finally recoils—were observed and quantified through correlations and power spectral densities.

Introduction

Applications for polymers tethered to surfaces are found in many areas of study. For example, polymer brushes—densely packed chains tethered to a surface at one end—aide in stabilizing colloids and in reducing friction between surfaces (i.e., providing lubrication in artificial joints).[1−3] Tethered polymers have varied uses in biological systems, such as DNA microarrays for diagnosis of mutations and creating biocompatible surfaces that reduce, or even eliminate, the element of nonspecific adsorption.[4−7]

In other contexts, noninteracting tethered polymers are useful in studying biological processes. The linear diffusion of a site-specific DNA-binding proteins in search of a target site on DNA has been studied by using shear flow to stretch tethered DNA chains.[8] However, the details of the DNA extension in shear flow were not considered. The extension will be a nonlinear function of the distance along the chain, and this will effect the diffusion of a protein along the chain.

Tethered DNA chains are also of use in creating microelectronic devices, such as scaffolds for creating molecular wires.[9] Future experiments, using metallized DNA scaffolds for creating contacts to organic single molecules, have been suggested to test the electrical properties of single organic molecules.[10,11] Single organic molecules are of great importance in the rapidly developing organic semiconductor industry, and these experiments would enable rapid screening of possible candidates. Short DNA chains (1−3 μm) are desired for ease of creating (organic molecule)−DNA complexes. At this length scale, the bending rigidity of the DNA backbone may play an important role in the shear flow processing.

All shear flow experiments to date have included examinations of fluorescent DNA chain dynamics in the flow-vorticity plane, affording no insight into chain dynamics very near the wall or in the flow-gradient plane.[12,13] In addition, previous simulations consist of mainly bead−spring models which may not capture the appropriate dynamics for short DNA segments.[12−14] Molecular dynamic simulations of short freely jointed chains have also been performed but were not completed for semiflexible chains such as DNA.[15]

*Corresponding author. E-mail: esgs@stanford.edu.

We will show that chain dynamics for tethered polymers are highly dependent on the bending modulus of semiflexible chains. Fluorescence microscopy experiments by Doyle et al. demonstrated the idea of cyclic dynamics for tethered DNA chains at moderate flow strengths.[12,13] Cyclic dynamics defines the process whereby the tethered polymer diffuses away from the wall and thus experiences high flow velocities, with subsequent extension of the polymer. The enhanced entropic force normal to the wall then creates a reduction in the distance from the wall and a recoil in the extension. Schroeder et al. used Brownian dynamics simulations to demonstrate the presence of a characteristic frequency for cyclic motion of a tethered polymer in shear flow when $1 < Wi < 10$ (where the Weissenberg number, Wi, is the shear rate times the longest polymer relaxation time).[14] Buscalioni examined the Wi regime of cyclic dynamics using bead−rod simulations of freely jointed chains.[15] However, bead−spring simulations and freely jointed bead−rod simulations do not completely incorporate the proper wormlike behavior of the chain. Experiments in the flow-gradient plane and Brownian dynamics simulations of semiflexible Kratky−Porod chains[16] are required to fully understand chain statistics.

Experimental Procedures

Viewing tethered DNA molecules in the flow-gradient plane under the influence of shear flow was accomplished by tethering one end of a fluorescently stained DNA molecule to the edge of a channel with a rectangular cross section (see Figure 1). The fluorescently stained DNA molecules were then visualized using a fluorescence microscope. To achieve successful visualization, we developed various procedures, modified from previous work, for tethering DNA molecules to a surface[12,13,17,18] and viewing fluorescent DNA molecules near sidewalls.[19]

Flow Cell Design. We first designed and constructed a flow cell where linear shear flow was observed on the scale of the radius of gyration of a tethered λ-phage DNA. Pressure-driven Poiseuille flow through a rectangular channel results in simple shear very near each wall.

Fused quartz coverslips, 250 μm × 25 mm × 25 mm, were purchased from Technical Glass Products, Inc., and 5 mm × 1 mm channels were laser etched 100 μm deep by Translume, Inc.

 Published on Web 11/02/2009

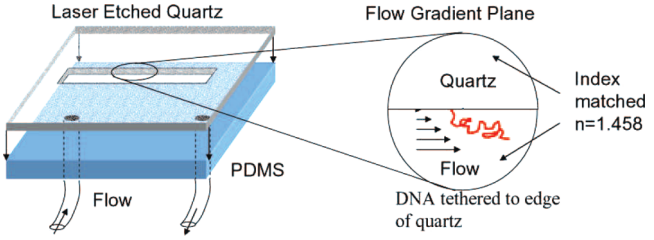

Figure 1. Diagram of flow-gradient cell. Laser etched quartz that has been treated for DNA tethering is placed on a PDMS backing. The refractive index of the flowing solution is matched to quartz to improve resolution in the flow-gradient plane. The perspective of the image on the right is from the top of the quartz slide looking into the laser etched channel at the interface between the flowing solution and the channel wall.

Because of the high cost of the laser etched fused quartz coverslips, all steps in creating a flow cell during an experiment were engineered to be reversible. For this reason, a polydimethylsiloxane backing (PDMS: Dow Corning Sylgard 184 silicone elastomer kit) was made that would adhere to the flow cell through a purely physical bond.

A Harvard Apparatus Pump 11 Pico Plus (PN: 702213), with the capability of infusion or extraction, was used with a 25 or 50 μL Hamilton 1700 series syringe with luer lock connections (PNs: 80222, 80920). Teflon tubing with a 360 μm outside diameter and a 150 μm inside diameter (PN: 1933) and appropriate luer lock fittings (PN: P-662) were purchased from Upchurch Scientific. Because of the flexibility of the Teflon tubing, which was needed to minimize transmission of vibrations from the pump to the flow cell, blunted 27 gauge needles were fixed to the ends using a 22 gauge sleeve and epoxy. The needles were subsequently forced into holes in the PDMS flow cell.

Refractive Index Matched Solution. Viewing fluorescently stained molecules near a vertical wall requires that the refractive index of the flowing solution be matched to the refractive index of the flow cell to prevent refraction-induced blurring. Sucrose has been previously used to increase the refractive index of aqueous solutions[19] to match the index of fused quartz. The refractive index of fused quartz is 1.4585 at 588 nm and 1.4633 at 500 nm.[20,21] The refractive index of sucrose solutions ranges from 1.4519 at 60% (m/m) sucrose in water to 1.4654 at 70% (m/m) sucrose in water.[22]

To obtain a refractive index of 1.4585 at 588 nm for the sucrose solution, 64.8 g of sucrose (Invitrogen UltraPure 15503-022) was added to 35.1 mL of 0.325 M Tris (Invitrogen 15568-025), 6.5 mM EDTA (Gibco ultraPURE: Invitrogen 15575-038), 32.5 mM NaCl (EMD SX0420-1), and 6.5 mg/mL β-D-glucose (EMD AnalaR: B10117−34) in Milli-Q water. The resultant solution had a viscosity of 261 ± 5 cP.

DNA Tethering. The second challenge was to create a reversible tethering process, where the quartz surface may be recovered upon cleaning. The biotin−streptavidin linkage was chosen to tether DNA molecules to surfaces, primarily due to the widespread literature on the subject, particularly in its use with biological systems.[23−25]

A piranha solution, 5:1 sulfuric acid (EMD SX1244-5) to hydrogen peroxide (EMD HX0635-6), was used to remove any carbon-containing molecules and create a hydrophilic surface. Slides were immersed in the piranha solution, and the activity of the reaction was sustained by further heating the mixture to 90 °C for 20 min.

In order to view single DNA molecules tethered to a surface, it is important that the fluorescently stained molecules be reasonably separated. This was accomplished by controlling the tethering density of DNA chains via limiting the number of binding sites for the biotinylated DNA molecules and later, limiting the exposure time of the biotinylated DNA to the avidin-activated surface. The former was regulated by adjusting the ratio of biotin-terminated PEG-NHS chains to methoxy-terminated PEG-NHS chains that react with an amine-functionalized surface.

Solution-phase deposition of an aminosilane was used due to the ease and quickness of the technique and the fact that the quality of the monolayer is less important than the accessibility of the amines for the PEGylation reactions. Quartz flow cells were immersed in a mixture of 2% (v/v) aminopropyltriethoxysilane (APTES) in hexanes for 15 min, quenched with ethanol, and dried under argon. Curing at 160 °C for 1 h at −27 in.Hg was also required to cross-link the APTES monolayer and create amine-functionalized surfaces that were stable in aqueous solvents.

Poly(ethylene glycol) (PEG) products, 5000 Da Biotin-PEG-NHS (SC, succinimidyl carbonate ester), and 5000 Da methoxy-PEG-NHS (SG, succinimidyl glutarate ester) were purchased from Creative PEGWorks (PNs: PLS-1922, PSB-220) and stored at −20 °C. Because of unwanted hydrolysis of the *N*-hydroxysuccinimide (NHS) ester to a carboxylic acid, NHS (Aldrich 130672-5G) and 1-ethyl-3-(3-dimethylaminopropyl)-carbodiimide (EDC: Acros 171440010) were also added to re-form the NHS ester. 30 μL of a solution containing 32 mM methoxypoly(ethylene glycol)−succidimidyl glutarate ester (mPEG-SG), 32 μM biotin−poly(ethylene glycol)−succinimidyl carbonate ester (BPEG-SC), 0.1 M NHS, and 0.4 M EDC in PBS buffer at pH 7.4 (Gibco 10010) was added to the amine-functionalized flow cells and placed in a dark box at 22 °C for 2 h. Dried flow cells were stored under argon for up to 1 month.

Biotinylated DNA was created by ligating λ-phage DNA (Invitrogen 25250-010) with the 12-mer biotin−oligomer (Operon 3′-[BioTEG-Q]CCCGCCGCTGGA-5′) containing a sequence complementary to a sticky end of λ-phage DNA. The T4 DNA ligase kit (M0202) and 100X bovine serum albumin (BSA) were purchased from New England BioLabs. Separation of unreacted oligomer from biotinylated DNA product was accomplished by repeated filtering with 100 kDa MW, 1.5 mL centrifuge filters purchased from Microcon (YM-100) in a Beckman Coulter Microfuge 18 centrifuge. Stored at 4 °C, biotinylated DNA remained active in excess of 2 years.

Prior to running a data acquisition experiment, a 30 μL drop of 1 mg/mL streptavidin in PBS pH 7.4 was placed on the PEGylated quartz flow-cell and placed in a dark box for 30 min at 4 °C. Following the assembly of the flow device, 1 μL of 0.05 mg/mL biotinylated λ-phage DNA was combined with 1 μL 10^{-4} M Sytox Green fluorescent dye from Molecular Probes (S7020) in 100 μL of Milli-Q water. The mixture and flow device were immediately removed from light, and the outlet line of the flow device was submerged in the stained DNA solution. The DNA solution was pulled through the flow device and allowed to tether in the flow cell for 5 min, immediately followed by injecting the sucrose solution using a 25 μL syringe. The sucrose flowing solution contained 233 μL of 65% sucrose buffer, 0.25 × 10^{-4} M Sytox, 1 μL of 50.8 mg/mL glucose oxidase (Sigma G714-250KU type X-S), 1 μL of 9.23 mg/mL catalase (Sigma C40-500MG), and 1 μL of β-mercaptoethanol for oxygen scavenging, to delay photobleaching of the fluorescent dye and cleavage of the DNA.

Microscope Setup. Imaging of single molecule λ-phage DNA was accomplished with a Nikon Eclipse TE300 epi-fluorescence microscope and a Photometrics Cascade 512B CCD camera. Light emitted from an EXFO X-Cite 120 mercury lamp was sent through a computer-controlled Sutter Instruments Lambda 10-B Smart Shutter and then a 480 ± 15 nm bandpass excitation filter (Nikon set B-2E/C F). A 505 nm long pass dichroic mirror reflects this light and sends it to a 100X α Plan FLUAR (Zeiss 1084-514) objective which focuses on the flow cell. The Sytox stained λ-phage DNA has a peak absorbance at 504 nm and peak emission at 523 nm. The emitted light is collected with the objective, sent through the dichroic mirror and the 535 ± 20 nm bandpass emission filter, and imaged with the CCD camera. Image capture software (Compix SimplePCI 6.0) was used to

take movies of the DNA dynamics. For λ-phage DNA experiments in 265 ± 5 cP, 65% sucrose solution, the time step between frames usually ranged from 3 s to 2 min. The lamp power was reduced to half power, and the exposure time for each frame was 100 ms in order to achieve a good signal-to-noise ratio for the stained DNA molecule.

Data Analysis. The image capture software was capable of exporting images of each frame that could then be imported to Matlab. An image analysis tool was written in Matlab that could extract chain statistics such as chain extension and the radius of gyration tensor. Data used in the calculation of chain statistics were restricted to the region containing intensities greater than a cutoff intensity (≈ 2 standard deviations of pixel intensities), defining a blob of interest which only contained the DNA. Because of the high speckle noise present in an image, a few filters were applied to the image prior to defining the blob of interest; however, chain statistics were only taken from the original, unfiltered intensities.

The chain extension is measured as the visible length of the chain in the flow direction and the radius of gyration tensor is defined as

$$G_{ij} \equiv \frac{\sum_{p,q} I(p,q)R_i(p,q)R_j(p,q)}{\sum_{p,q} I(p,q)} \tag{1}$$

where I is the intensity and R_i is the position with respect to the tethering point for pixel at row p and column q. A component of R in the 1-direction is defined to be in the direction of the flow and the 2-direction is defined to be normal to the surface.

From the radius of gyration tensor, we define the root-mean-square distance from the wall, δ_2, and the orientation angle of the polymer with the surface, ϕ, as

$$\delta_2 = \sqrt{G_{22} - \delta^2_{\text{resolution}}} \tag{2}$$

$$\tan 2\phi = \frac{2G_{12}}{G_{11} - G_{22}} \tag{3}$$

where $\delta_{\text{resolution}}$ is associated with the widening of the distribution due to the optical resolution of our microscope as calculated by measuring the width of a fully extended DNA, which should in actuality have negligible thickness. The orientation angle, ϕ, is equivalent to the angle between the surface and the intensity-weighted least-squares fit through the image that passes through the tethering point.

Simulation Procedures

The dynamics of a double-stranded DNA molecule longer than 100 base pair (34 nm) are well reproduced by a Kratky−Porod chain model,[26] which represents the chain as discrete rigid segments with a bending potential to induce wormlike chain behavior.[16,27] However, due to current computational limitations of Brownian dynamics simulations, the chain length of full Kratky−Porod simulations has been restricted to less than 10−20 kbp (3.4−6.8 μm). For longer chains, bead−spring simulations have been used.[12−14,28] Bead−spring models reproduce force−extension statistics of wormlike chains but do not include bending constraints. Under shear flow, small fluctuations normal to the surface induce large fluctuations in extension, and therefore, the reliability of such coarse-grained bead−spring simulations is unclear. Kratky−Porod simulations were used to understand the limitations of coarse-grained bead−spring simulations, used for modeling λ-phage DNA.

Kratky−Porod Bead−Rod Model. The Kratky−Porod model is a modified version of the Kramer's freely jointed bead−rod chain model[27] that includes the bending modulus. This is the model from which the wormlike entropic spring force law, eq 13, is derived.[29] The polymer chain is represented by a bead−rod chain with many more segments, $N - 1$, than Kuhn steps, N_k. In this way it is possible to allow the bending modulus to control the persistence length, regardless of the discretization of the chain.[30]

The Langevin equation describes the motion of Brownian particles in solution. A force balance for each bead (i) in a system of N particles yields the Langevin equation. Ignoring bead inertia, the Langevin equation can be transformed into a stochastic differential equation for the position, R_i, of each bead in the chain.

$$\frac{d\mathbf{R}_i}{dt} = \mathbf{u}_i^\infty + \frac{1}{\zeta}(\mathbf{F}_i^W + \mathbf{F}_i^C + \mathbf{F}_i^T) + \sqrt{\frac{2k_BT}{\zeta}}\mathbf{W}_i \tag{4}$$

where $\mathbf{u}_i^\infty$ is the fluid velocity in the absence of particles:

$$\mathbf{u}_i^\infty = \begin{bmatrix} 0 & \dot{\gamma} & 0 \\ 0 & 0 & 0 \\ 0 & 0 & 0 \end{bmatrix} \cdot \mathbf{R}_i \tag{5}$$

in shear flow. ζ is the bead resistivity; $\mathbf{F}_i^W$ represents force contributions from the wall, $\mathbf{F}_i^C$ represents bending within the chain, and $\mathbf{F}_i^T$ represents a tension between adjacent beads; and $\mathbf{W}_i$ is a Wiener process[30] such that

$$\langle \mathbf{W}_i \rangle = 0 \tag{6}$$

$$\langle \mathbf{W}_i(t)\mathbf{W}_j(t+dt) \rangle = \delta_{ij}\delta(dt) \approx \frac{\delta_{ij}}{dt} \tag{7}$$

where δ_{ij} is the second-order isotropic tensor between beads i and j and δ is the Dirac delta function. To implement this random Brownian force, a Gaussian distributed random number satisfying these constraints was generated.

The tension forces, needed to keep the rod lengths fixed, are unknown a priori and are calculated iteratively using Picard's method[28,31] until the following constraint is satisfied:

$$||\mathbf{Q}_i| - l| < \varepsilon \tag{8}$$

where $\mathbf{Q}_i$ is the connector vector between beads i and $i+1$, l is the length of the discretized rod segment, and ε is chosen to be $l \times 10^{-6}$.

A stiffer wall force

$$\mathbf{F}_j^W = \begin{cases} C_W k_B T \left(\dfrac{1}{\exp[5h_j/\delta_W] - 1} - \dfrac{1}{\exp[5] - 1} \right)\mathbf{n}; & h_j < \delta_W \\ \mathbf{0}; & h_j \geq \delta_W \end{cases} \tag{9}$$

than previously used for Brownian dynamics simulations[32,33] can be implemented with the addition of an adaptive time step algorithm. This will help improve the dynamics of the chain very near the wall. The boundary thickness is again

chosen to be very small, $\delta_W = 0.03l = (1/100)R_g$, and C_W is chosen to be comparable to other bending and tension forces. Discretization of the bending force for a continuous chain yields

$$\mathbf{F}_i^C = \frac{\hat{l}_P}{l} k_B T \begin{cases} -\mathbf{R}_{i-2} + 4\mathbf{R}_{i-1} - 6\mathbf{R}_i + 4\mathbf{R}_{i+1} - \mathbf{R}_{i+2}; & 3 \le i \le N-2 \\ 2\mathbf{R}_{i\mp1} - 5\mathbf{R}_i + 4\mathbf{R}_{i\pm1} - \mathbf{R}_{i\pm2}; & i = 2(\text{top}),\ N-1(\text{bot}) \\ -\mathbf{R}_i + 2\mathbf{R}_{i\pm1} - \mathbf{R}_{i\pm2}; & i = 1(+),\ N(-) \end{cases} \tag{10}$$

where $\hat{l}_P$ is the persistence length of the chain in the limit of infinite bead number.[34,35] For finite chains, the actual persistence length, l_P, can be calculated by fitting simulation results for the chain tangent autocorrelation function.

$$\langle \mathbf{Q}_1 \cdot \mathbf{Q}_i \rangle = \exp\left[-\frac{(i-1)l}{l_P} \right] \tag{11}$$

Thus, the actual persistence length of the chain is known and N or l_P is determined iteratively to reproduce the appropriate number of Kuhn steps.

Bead−Spring Model. The bead−spring chain consist of a series of Brownian particles held together by entropic springs. Ermak and McCammon[36] developed an equation for the spatial evolution of hydrodynamically interacting Brownian particles under constraining forces. For 150 Kuhn step λ-DNA, it has been shown that hydrodynamic interactions are rather insignificant in shear and extensional flow;[37] therefore, it follows that for a 22 Kuhn step chain far from equilibrium hydrodynamic interactions can be safely neglected in free solution. However, it may be of interest to examine the effects of hydrodynamic interactions due to the presence of a surface. Here, it is assumed that the entropic exclusion force shown in eq 21 will dominate over hydrodynamic interactions. A system of stochastic differential equations describing the positions, $\mathbf{R}$, of freely draining interacting beads, $i = 1, 2, ..., N$, is as follows:[30]

$$d\mathbf{R}_i = \begin{cases} 0; & i = 1 \\ \left(\mathbf{u}_i^\infty + \frac{1}{\zeta}(\mathbf{F}_i^{HS} - \mathbf{F}_{i-1}^{HS}) \right) dt + \sqrt{\frac{2k_B T}{\zeta}}\, d\mathbf{W}_i; & i = 2 : N-1 \\ \left(\mathbf{u}_i^\infty + \frac{1}{\zeta}(\mathbf{F}_{i-1}^{HS}) \right) dt + \sqrt{\frac{2k_B T}{\zeta}}\, d\mathbf{W}_i; & i = N \end{cases} \tag{12}$$

This results from a balance between disturbances caused by the free stream velocity, $\mathbf{u}_i^\infty$; a half-space entropic force, $\mathbf{F}_i^{HS}$; and solvent−bead collisions expressed as an isotropic Wiener process, $d\mathbf{W}_i$.[30] Each spatial component of $d\mathbf{W}_i$ is modeled as a Gaussian random number with a variance of dt.[28] The first bead in the chain is tethered to the wall and accordingly has no net disturbance. Note that while this model captures the correct extensional force of the wormlike chain using the appropriate spring force, $\mathbf{F}_i^W$, as discussed below, it does not capture the appropriate bending modulus over the length of the chain.[29,38]

The only nonzero component of the free stream velocity is defined to be that for flow in the x-direction, whereas the wall normal is defined to be in the y-direction, resulting in $\mathbf{u}_i^\infty = \dot{\gamma}[y,0,0]$, where $\dot{\gamma}$ is the shear rate.

At equilibrium, there are far more chain conformations in a coiled state than in a stretched state. In order to perturb the equilibrium coil, a force is applied to opposite ends of the chain. Therefore, there exists an entropic restoring force pulling the ends of the chain back together. A force law has been developed for a wormlike chain by Marko and Siggia[29,38] and is used for the entropic spring force between consecutive beads of a bead−spring chain in free solution.

$$\mathbf{F}_i^S = f\left(\frac{Q_i}{L}\right)\frac{\mathbf{Q}_i}{Q_i} \tag{13}$$

$$f\left(\frac{Q_i}{L}\right) = \frac{k_B T}{4l_P}\left(\frac{1}{(1-Q_i/L)^2} - 1 + 4\frac{Q_i}{L} \right) \tag{14}$$

However, the presence of a wall changes the available conformations of the chain represented by a spring. To eliminate all conformations that penetrate the surface, the probability function for a Gaussian chain or a freely jointed chain can be calculatedby implementing a zero probability or reflective boundary condition.[39] The reasoning is outlined in Figure 2. Given that the chain starts at point "A", the conformation "CB" has equal probability to conformation "*CB*" and a reflective boundary condition is necessary and sufficient. The probability in the presence of the wall, conformation "AB" not through "C", can be defined in terms of the free space probability, as

$$P^{HS}(AB) = P(AB) - P(AB^*) \tag{15}$$

The magnitude of the reflected connector vector between A and B^*, Q^{*2}, is defined by a set of equations

$$Q^{*2} = Q_\parallel{}^2 + (\varepsilon_A + \varepsilon_B)^2 \tag{16}$$

$$Q_\parallel{}^2 = Q^2 - Q_\perp{}^2 \tag{17}$$

$$Q_\perp = \varepsilon_B - \varepsilon_A \tag{18}$$

where $Q_\parallel$ is the component of Q parallel to the surface and $Q_\perp$ is the component perpendicular to the surface. Subsequently, the half-space entropic force associated with the chain end, B, assuming the chain begins at a fixed point, A, is

$$\mathbf{F}_B^{HS}(\mathbf{Q}, \varepsilon_A) = k_B T \frac{\partial \ln[P(Q) - P(\sqrt{Q^2 + 4\varepsilon_A \varepsilon_B})]}{\partial \mathbf{Q}}\bigg|_{\varepsilon_A} \tag{19}$$

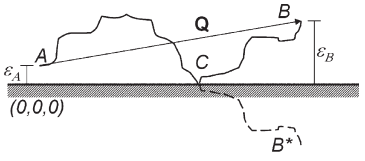

Figure 2. Method of reflection: probability near a surface. Probability of a random walk, starting at A, reaching B by subtracting the probability of reaching B^* (the reflection of B). The probability of reaching B from C is equivalent to that of reaching B^* from C.

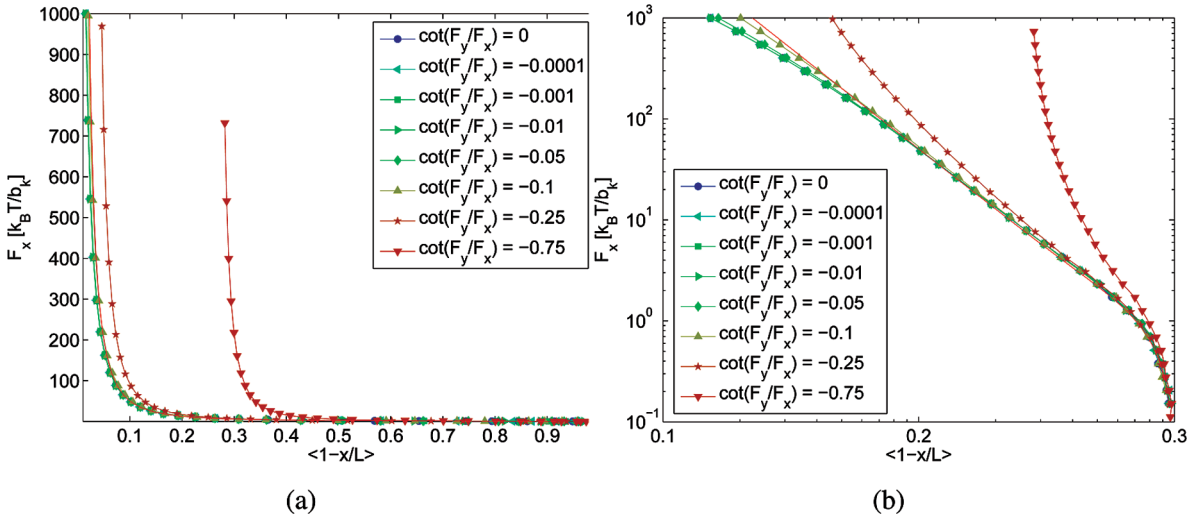

Figure 3. Force vs dimensionless extension deficit near a surface: Kratky−Porod Monte Carlo force in direction parallel to the wall vs extension deficit in the same direction. Different symbols represent different angles at which the force is applied, with increasingly negative angles being pulled into the wall. The solid curve represents the expected wormlike chain behavior in free solution.

As the chain approaches the surface, $4\varepsilon_A\varepsilon_B \ll Q^2$, a Taylor series approximation yields

$$\mathbf{F}_B^{\mathrm{HS}} = \left(-f(|\mathbf{Q}|) - \frac{k_\mathrm{B}T}{|\mathbf{Q}|} + k_\mathrm{B}T\frac{\partial \ln f(\mathbf{Q})}{\partial|\mathbf{Q}|}\right)\frac{\mathbf{Q}}{|\mathbf{Q}|} + k_\mathrm{B}T\frac{\mathbf{n}}{\varepsilon_B} \tag{20}$$

where **n** is the unit vector normal to the surface. For the purposes of long tethered DNA chains in shear flow, the dominating terms are the first term, significant close to the wall, and last term, significant at high extension. The last term is responsible for keeping the chain away from the wall.

For a wormlike chain, however, the stiffness requires that we enforce a zero flux condition as well as a zero probability condition. In other words, given "A", the conformation "CB" does not have equal probability to conformation "*CB**", due to the discontinuity in the chain contour at C. Therefore, the half-space probability function is not easily defined in terms of the free-solution chain distribution. The probability distribution has been studied previously using confocal microscopy of tethered DNA molecules,[40] but no closed form for the probability distribution function existed at the time. The authors used an approximation that, for chains longer than about 20 Kuhn steps, is equivalent to a Gaussian distribution with a reflective boundary condition. This approximation did not have a major impact on their results, as they were using the distribution to fit the radius of gyration and analyze scaling with chain length.

Here, Monte Carlo simulations utilizing a Metropolis algorithm were used to determine the effects on the half-space entropic force law and probability distribution for a tethered chain. Forces parallel to the surface and toward the surface were applied to the chain end, while determining its average position in each direction. Position versus applied force is plotted in Figure 3 and Figure 4.

By fitting to simulation results in Figure 4, we see that the more exclusive character of the wormlike chain results in a half-space entropic force of the form

$$\mathbf{F}_i^{\mathrm{HS}} = -f(|\mathbf{Q}_i|)\frac{\mathbf{Q}_i}{|\mathbf{Q}_i|} + 2k_\mathrm{B}T\frac{\mathbf{n}}{\mathbf{R}_{i+1}\cdot\mathbf{n}} \tag{21}$$

acting on bead $i + 1$ as a consequence of spring i. An analogous calculation is repeated for the force on bead i as a result of spring i.

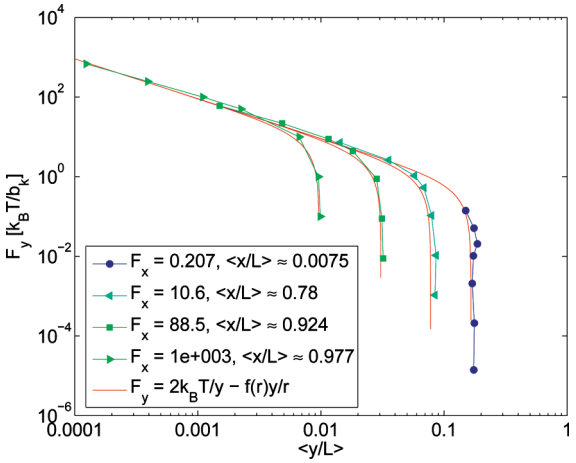

Figure 4. Force vs distance from the wall: Kratky−Porod Monte Carlo force applied to the chain end pulling into the wall verses average distance from the wall. Different data curves represent varying forces in the direction parallel to the surface from 0.11−1000 $k_\mathrm{B}T/b_\mathrm{k}$. Solid curves represent the prediction of eq 21 at a given extension, x, approximately representing mean extension at an applied force, F_x.

A general predictor−corrector method is used for solving eq 12.[28,32,42] The difference here lies in the half-space entropic force containing a component that is not in the direction of extension, eq 21. The entropic wall exclusion force normal to the surface is separated from the spring force parallel to the spring and incorporated into the algorithm as if it were a body force similar to the drag force.

To ensure that a Brownian fluctuation will not force a bead through the wall, an adaptive time step was again implemented. For calculating the end-wall contact frequency, contact with the wall is made if a bead comes within a distance of $R_\mathrm{g}/10000$. Scaling of contact frequency with Wi was independent of this value, as long as it was much less than the radius of gyration of a spring.

Results

Kratky−Porod vs Bead−Spring. On the basis of Kratky−Porod Monte Carlo simulations, in order to accurately represent a 22 Kuhn step DNA chain at high extension (95%), one must include at least 300 discretized segments.

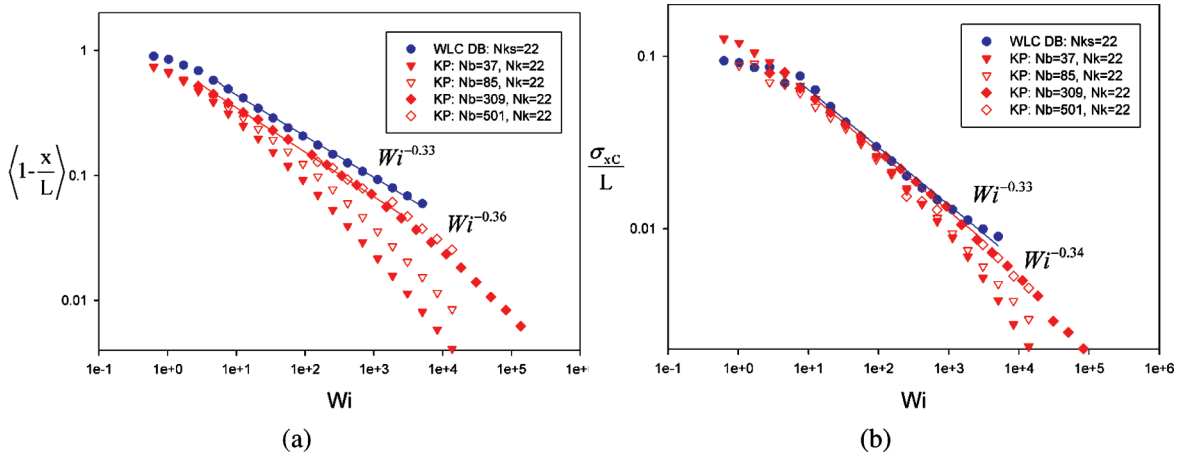

Figure 5. Kratky–Porod and WLC bead–spring: extension vs *Wi* dimensionless extension deficit (a) and dimensionless standard deviation in extension (b) are shown to approach scalings of bead–spring simulations with increasing number of modes. When more modes are included, the Kratky–Porod chain displays less freely jointed behavior and more wormlike behavior.

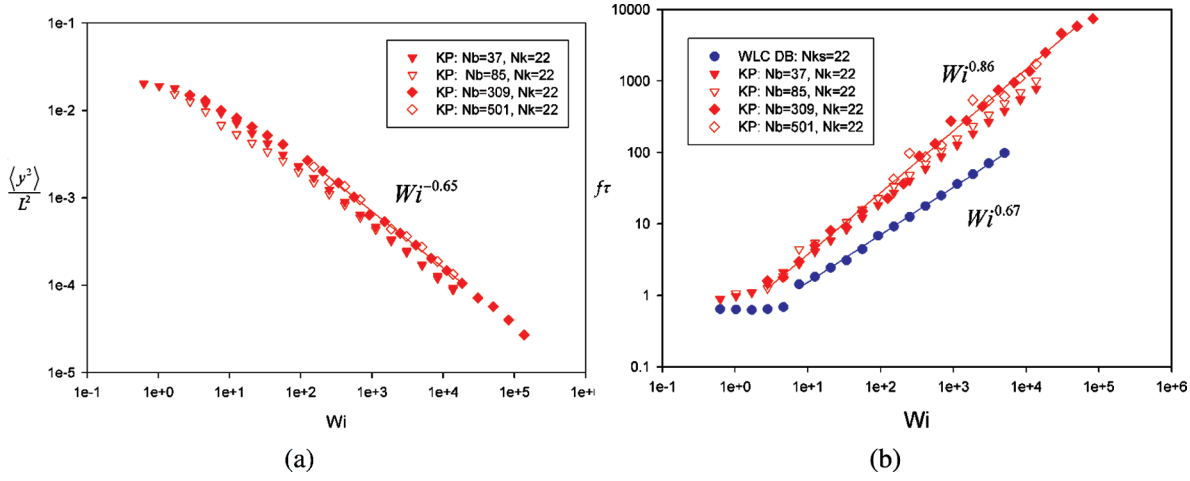

Figure 6. Distance from wall and contact frequency vs *Wi* dimensionless mean-square distance from the wall (a) scales consistently as predicted, regardless of discretization. (b) Kratky–Porod simulations of chain end–wall contact scale differently from dumbbell simulations and predictions.

Therefore, λ-phage DNA of 153 Kuhn steps would require more than 2000 discretization segments, and these simulations would require months to run on a single processor. On the other hand, bead–spring simulations require much less computation time and require fewer degrees of freedom to represent the same chain. However, the entropic force law is derived for a polymer at equilibrium and may not remain reliable for a polymer in shear flow near a surface.

In order to determine the limitations of the bead–spring model, we modeled a 22 Kuhn step (proposed length for DNA–organic molecule complexes) wormlike chain tethered to a surface in shear flow. We examine scaling of extension deficit (contour length minus extension), extension standard deviation, and root-mean-square distance from the wall versus flow strength, $W_i = \dot{\gamma}\tau$, where $\dot{\gamma}$ is the shear rate and τ is the longest relaxation time measured by extension–relaxation[42] parallel to the surface. Extension deficit, extension standard deviation, and root-mean-square distance from the wall have all been shown to scale as $W^{-1/3}$ for a wormlike chain.[12,13] However, extension deficit and standard deviation will scale as $Wi^{-2/3}$ for a freely jointed chain.[12,13] For purposes of double tethering DNA to a surface, it is also of interest to analyze chain end–wall contact frequency versus flow strength. Assuming contact of the chain end with the wall is a diffusive process from the average distance from the wall, the contact frequency should scale like $Wi^{2/3}$.

Figure 5a shows a plot of the extension deficit, $1 - \langle x\rangle/l$, versus Weissenberg number, *Wi*. It is apparent that dumbbell simulations are in agreement with scaling prediction of $Wi^{-1/3}$. The slight overprediction in the magnitude of the scaling factor for extension deficit, −0.36, and standard deviation in extension, −0.34, is caused by discretization at the highest *Wi* and the corresponding deviation in the force–extension curve at high extension.

Figure 6a shows the mean-square distance of the chain end from the surface scaling as predicted $Wi^{-2/3}$. This is true regardless of discretization because the chain's mean distance from the wall is completely independent of the force law (or chain character). Interestingly, the scaling even holds for length scales that are orders of magnitude shorter than the Kuhn step length ($\langle y^2\rangle/L^2 \ll 0.002$).

On the other hand, Kratky–Porod simulations shown in Figure 5 produce a different frequency of bead–chain contact scaling as $Wi^{0.86}$ rather than calculated from bead–spring simulations and our predictions of $Wi^{2/3}$ from the dumbbell model. There are two possible explanations. First, the entropic forces will have an effect on end–wall contact, rather than being purely diffusive. Second, the diffusivity of the chain end is higher than that of an element within the

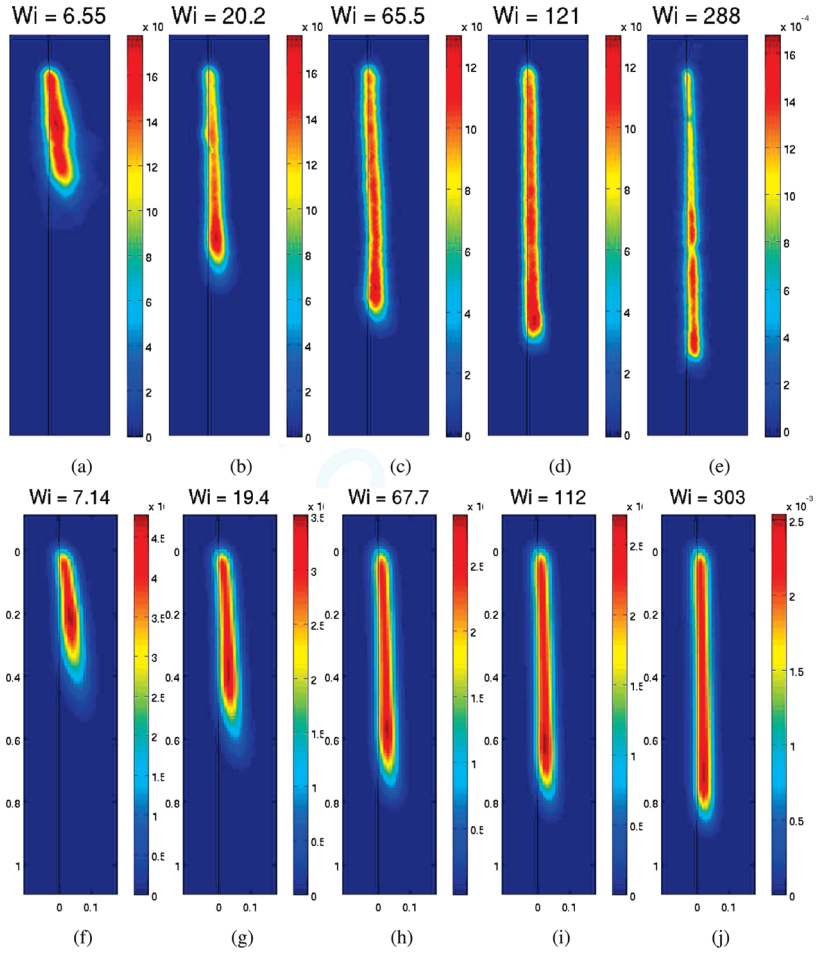

Figure 7. Ensemble images of λ-DNA and bead−spring simulations (a−e) Ensemble images are created by extracting a region of interest for each frame captured and summing all regions for one molecule. (f, g) Bead−spring simulation comparisons at similar flow rates were transformed with a Gaussian filter for viewing. The height of each image is 120% of full extension (21 μm for the experimental images).

chain, and as the chain itself gets closer to the wall, it becomes increasingly easier for the chain end to contact the wall. Both of these effects should be present for all chains, whether they are freely jointed or wormlike. As a consequence of a higher scaling factor for bead−rod chains as compared to a dumbbell, the chain will contact the surface more frequently than predicted and will be beneficial for purposes of double-tethering DNA and creating molecular wires. This scaling discrepancy is worth further study and may be highly correlated with the scaling of the cyclic dynamics frequency, which would be of consequence to previous predictions.[14]

Experimental Comparison: Shear Rate Dependence. Visualizing tethered DNA molecules in the flow-gradient plane provides a direct test of molecular theories and Brownian dynamics simulations. Weak and strong flows were considered, and data for the polymer extension, standard deviation in extension, distance from the wall, and orientation angle were collected and examined to determine the dependence on flow strength, Weissenberg number (Wi). For moderate flows the presence of cyclic dynamics was explored. To reiterate, cyclic dynamics is the process of extension and recoil driven by chain distance from the surface. Extension, height (distance from the wall), and angle autocorrelation functions and extension−height cross-correlation functions were inspected for the presence of a characteristic frequency of cyclic motion as predicted elsewhere.[14,15]

The length of λ-DNA stained with Sytox-Green at 10^{-7} M was measured to be 17.3 ± 0.5 μm by using high shear rates to stretch out the chain to near full extension. Dyes used in other studies, such as YOYO and TOTO, may yield different contour lengths due to different degrees of intercalation of the dye within the DNA.[14,19,42] The relaxation time for the tethered DNA in the 261 cP sucrose solution was found to be 52.5 s by extension−relaxation experiments[42] parallel to the surface. The strength of the flow was gauged in relation to the relaxation time by calculating the dimensionless parameter $Wi = \dot{\gamma}\tau$. The effect of flow strength on the tethered polymer's conformation in the flow-gradient plane under the influence of shear flow was examined in detail. Two-dimensional distributions in the flow-gradient plane are shown in Figure 7 for both λ-phage DNA experiments and $N = 20$ bead−spring simulations. Distributions from bead−spring simulations needed modification to create comparable images. First, points were interpolated between adjacent bead positions to create the appearance of a continuous chain. Second, a Gaussian filter was applied to the simulation data on the same order of the optical resolution of the microscope to create qualitatively comparable images. By comparing ensemble-averaged images between simulations and experiments, we see a qualitative agreement of extension versus Wi. At the lowest flow rate, the experiments and simulations show an intense peak in the middle of the distribution and lower intensity near the end, due to the presence of cyclic dynamics. A few notable discrepancies are found between the simulation and experimental images. The first is that experiments images seem to be more highly peaked at the end of the

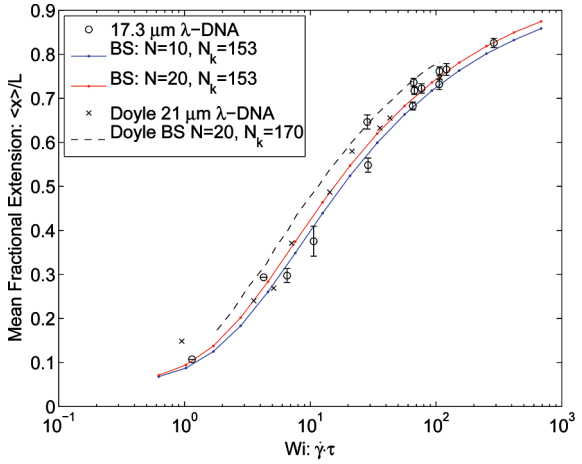

Figure 8. Extension vs flow strength. Experimental results for 17.3 μm λ-phage DNA are in good agreement with bead−spring simulations of free-draining wormlike chains consisting of 153 Kuhn steps and previous simulations and experiments by Doyle.[13]

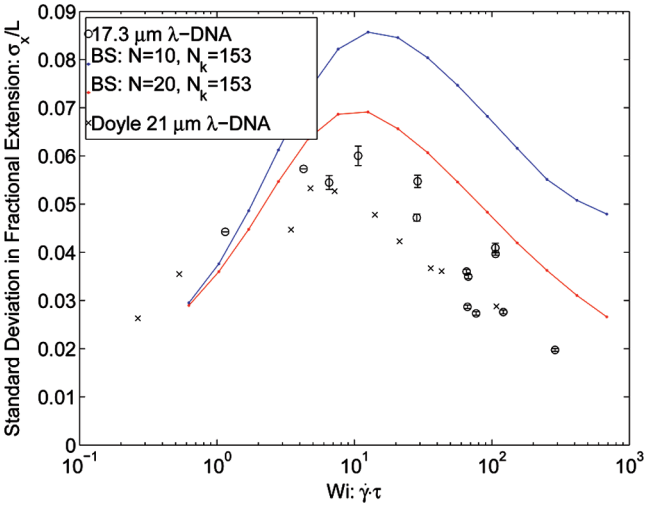

Figure 9. Extension fluctuations vs flow strength. Experimental results for 17.3 μm λ-phage DNA show smaller fluctuations than bead−spring simulations of 153 Kuhn step free-draining wormlike chains. Increasing the number of modes used to discretize the chain in a simulation has the effect of decreasing extensional fluctuations. For all chains studied, peaks in the curves were observed near $Wi \approx 10$, where interplay between diffusion and flow strength was greatest, in agreement with Doyle.[13]

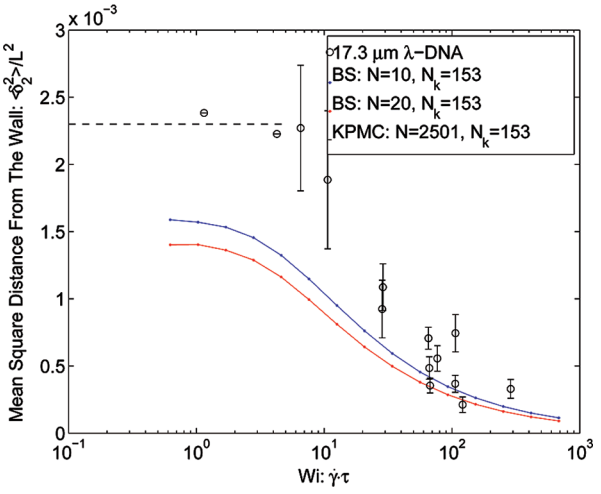

Figure 10. Mean-square distance from the wall vs flow strength. Experimental results for 17.3 μm λ-phage DNA show larger mean-square distances than do bead−spring simulations of $N_k = 153$ but agree with predictions made using Kratky−Porod Monte Carlo simulations near $Wi = 0$.

chain than do the simulations. Second, and somewhat related, extensional fluctuations seem to be higher in bead−spring simulations as visible by a spreading of the distribution near the end of the chain. Both discrepancies are most likely due to the discretization used in the bead−spring simulations.

The average extension of a tethered λ-phage DNA molecule is shown in Figure 8 versus *Wi*. A comparison is also made with bead−spring simulations of 153 Kuhn step wormlike chains and to previous experimental and simulation results from Doyle.[13] Error bars are calculated as standard errors at the 95% confidence limit assuming data becomes uncorrelated on the order of a relaxation time. Averages are calculated using a time series of a single DNA as well as an average over multiple DNA molecules. Larger errors are generally associated with averaging over fewer DNA molecules. The extension of a polymer in free shear flow is known to plateau around 50% of its contour length because of the tumbling dynamics.[14,19] However, when the polymer is tethered, it is allowed to reach full extension at high *Wi* because the probability of recoil decreases and tumbling does not exist.

Upon increasing the flow strength, a change in the relative probabilities of restretch and recoil have the effect of changing the size of the fluctuations in extension. The standard deviation in extension is plotted in Figure 9. There exists an obvious discrepancy between bead−spring simulations and experiments. Bead−spring simulations consistently overpredict extensional fluctuations. The entropic spring force assumes an equilibrium chain distribution, whereas in reality, fluctuations in chain conformation normal to the surface will be greatly reduced, in effect stiffening the chain and reducing extensional fluctuations. This argument is supported by the variation found between simulations at different levels of discretization, where increasing number of modes results in better agreement with experiments. In all cases, a maximum is reached near $Wi \approx 10$, where competition between the flow strength parallel to the wall and polymer diffusion perpendicular to the wall is greatest. This is in agreement with Doyle's observed peak in the standard deviation at $Wi = 5.1$[13] because the relaxation time was calculated from the autocorrelation function of extension at equilibrium, which was generally observed in simulations to be half as large as that calculated via extension−relaxation. At higher flow strength, beyond this peak, the region of recoil is reduced and extensional fluctuations decrease. Extensional fluctuations at low *Wi* are also small because the flow is not strong enough to greatly perturb the equilibrium distance of the polymer from the wall. This observation is shown in Figure 10.

The polymer mean-square distance from the wall as shown in Figure 10 begins to decrease near $Wi \approx 3-4$. The chain distance from the wall was defined by eq 2 from the radius of gyration tensor around the tethering point. Increasing the *Wi* and, therefore, increasing the extension creates an entropic penalty for diffusion perpendicular to the wall.

There is significant disagreement between bead−spring simulations and experiments at low *Wi*. The distribution of chain distance from the wall differs qualitatively between wormlike and freely jointed chains. Wormlike chains are excluded from the wallsmore readily than freely jointed chains, which will result in larger average distances from the wall. Experimental results at low *Wi* are in agreement

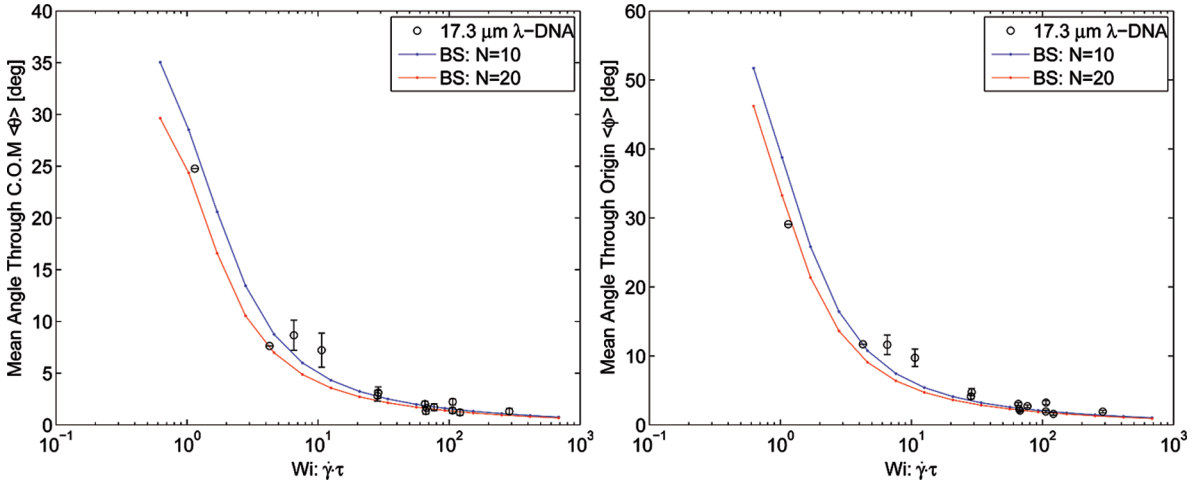

Figure 11. Orientation angle vs flow strength. Experimental results for 17.3 μm λ-phage DNA reveal larger orientation angles than do bead−spring simulations of $N_k = 153$. The orientation angle experiences a sharp decay up to $Wi \approx 10$ due to an increase in extension and a decrease in height. Similar trends are for the orientation angle through the origin and through the center of mass, with a consistently larger angle through the origin.

with the mean-square distance from the wall as calculated using equilibrium Kratky−Porod Monte Carlo simulations for $N = 2501$ beads and $N = 1901$ beads representing $N_k = 153$ Kuhn steps. Bead−spring simulations using the half-space entropic spring force, which includes the proper wall exclusion force, exhibit a character that is a combination of a wormlike chain and a freely jointed chain. The wall exclusion force is only effective at the length scale of a single spring. At longer length scales, the wall exclusion will be driven by the freely jointed nature of the bead−spring chain itself.

To calculate the radius of gyration in the wall-normal direction, we begin by examining a Gaussian distribution that is modified by either a zero probability or zero flux boundary condition for a freely jointed or wormlike chain, respectively (see eqs 20 and 21). A wall exclusion force of k_BT/y produces a distribution that has a multiplier of y, whereas an exclusion force of $2k_BT/y$ yields a multiplier of y^2. While making a simplification that the free chain approximately satisfies a Gaussian distribution, $G_\sigma(x,y,z)$; an approximate tethered freely jointed chain distribution, $P(x,y,z) = yG_\sigma(x,y,z)$; and an approximate tethered WLC distribution, $P(x,y,z) = y^2G_\sigma(x,y,z)$, are found. Consequently, mean distances from the wall of σ, 2σ, and 3σ are obtained for the free space, tethered freely jointed, and tethered wormlike chains, respectively. Since this relation should work at any length scale along the polymer chain greater than 10 Kuhn steps, the radius of gyration will scale in an identical fashion. The radius of gyration of a polymer calculated from its center of mass is $\langle R_g^2\rangle = N_k b_k^2/6$. Assuming that calculating the radius of gyration from an end is equivalent to calculating the radius of gyration for a polymer with twice the length, we find $\langle R_g^2\rangle = 2N_k b_k^2/6$. The mean-square distance in one direction is 1/3 of the radius of gyration, $\langle \delta_2^2\rangle = N_k b_k^2/9$. Using this formula and the coefficients found previously, the mean-square height, enforcing different wall entropic-exclusion forces, is

$$\frac{\langle \delta_2^2\rangle}{L^2} = \frac{1}{9N_k}; \quad F_{2,\text{wall}} = 0 \tag{22}$$

$$\frac{\langle \delta_2^2\rangle}{L^2} = \frac{2}{9N_k}; \quad F_{2,\text{wall}} = \frac{k_BT}{R_2} \tag{23}$$

$$\frac{\langle \delta_2^2\rangle}{L^2} = \frac{1}{3N_k}; \quad F_{2,\text{wall}} = 2\frac{k_BT}{R_2} \tag{24}$$

Calculating the equilibrium mean-square height (distance from the wall) for a 153 Kuhn step chain tethered to a surface, we find a mean-square height of $\langle \delta_2^2\rangle/L^2 = 0.0022$ for a wormlike chain, which is in agreement with Monte Carlo simulations value of 0.0023 ± 0.0001. Alternatively, we find a mean-square height of $\langle \delta_2^2\rangle/L^2 = 0.0015$ for a freely jointed chain. These results support the explanation for the discrepancy at low Wi between λ-phage DNA experiments and bead−rod simulations shown in Figure 10.

The orientation angles through the center of mass (Figure 11a) and through the tethering point (Figure 11b) are shown to decay rapidly even at low shear rates. The orientation angle, ϕ, through the tethering point (origin) drops rapidly from 90° to approximately 10° at 4−10 Wi. The orientation angle, θ, through the center of mass (COM) was invariably less than ϕ. Because of the entropic penalty of the chain being in close proximity to the wall, the majority of the chain is forced out into the fluid. With the competing drag force, the chain becomes restricted to an L-shaped region, causing $\theta < \phi$.

Experimental Comparison: Strain Dependence and Cyclic Dynamics. Since we have developed a sufficient understanding of the average dynamic properties for tethered polymers in shear flow at varying Wi, temporal fluctuations can now also be analyzed. Based on simulation results, at intermediate shear rates relative to the polymer relaxation time, $3 < Wi < 200$, the competition between flow-induced drag on the polymer and Brownian diffusion result in cyclic dynamics. Cyclic dynamics denotes the behavior of restretch and recoil introduced earlier.

Figure 12 shows experimental time traces of chain height, extension, orientation angle, and the corresponding chain images in the flow gradient plane. Cyclic dynamics are observed at $Wi \approx 4.3 \pm 0.2$ and is most obvious by comparing trajectories of chain height and extension. The dashed lines connecting points A, B, C, D, E, and F in Figure 12a outline the oscillatory behavior in the chain height. Dashed lines connecting corresponding points A*, B*, C*, D*, E*, and F* in Figure 12b outline oscillatory behavior in the chain extension. There is a consistent delay in the polymer extension relative to an increase in height which will later be quantified through their cross-correlation function. The polymer diffuses away from the surface, into higher velocity fluid, and thus experiences a larger drag force. This results in chain extension

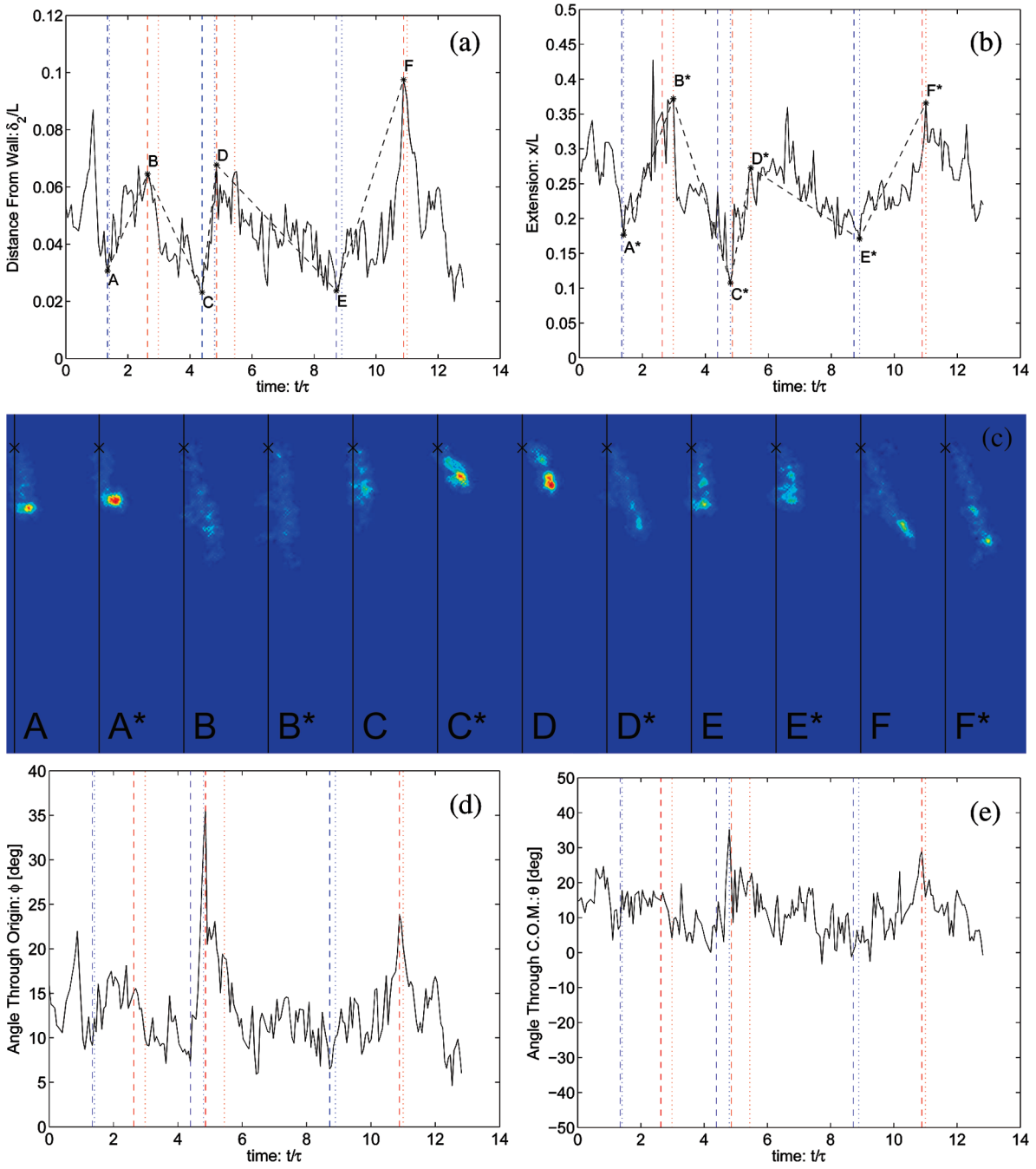

Figure 12. Cyclic dynamics at $Wi \approx 4.3 \pm 0.2$. 17.3 μm λ DNA tethered in shear flow experiences a cycle of thickening ($A \rightarrow B$, $C \rightarrow D$, $E \rightarrow F$), extension ($A^* \rightarrow B$, $C^* \rightarrow D$, $E^* \rightarrow F^*$), thinning ($B \rightarrow C$, $D \rightarrow E$), and recoil ($B^* \rightarrow C^*$, $D^* \rightarrow E^*$). Extension follows thickening at a short time delay ($B \rightarrow B^*$, $C \rightarrow C^*$); however, thinning is less correlated to extension ($B^* \rightarrow C$, $C^* \rightarrow D$). The height of the image in (c) is 21 μm.

over a time scale governed by the inverse shear rate. The increase in extension reduces the available conformations of the polymer and reduces the projection of the chain in the gradient direction, B−C and D−E. Images shown in Figure 12 illustrate all three cycles. The fluorescent microscope was capable of capturing higher quality images; however, to aid with collecting large time series, very low light intensities were used in the data acquisition. As shown in Figure 12, orientation angles through the center of mass and through the tethering point both show large fluctuations when the projection in the gradient direction is large, e.g., at points B and D.

Correlation functions of these variables and their power spectral density functions can be used to examine the presence of quasiperiodicity. Quasiperiodic motion is often defined as "the type of motion executed by a dynamical system containing two incommensurate frequencies".[43] Here we define quasiperiodic as motion containing a dominant, nonzero frequency with other incommensurate frequencies.

Experimentally, because of photobleaching of fluorescently stained DNA which results in cleavage, between 300 and 600 snapshots at an exposure time of 0.15−0.3 s could be taken of one molecule. When compared to steady-state averages from Figures 8 through 11b, larger ensembles were needed for correlation function calculations due to the small features characteristic of quasiperiodicity. Therefore, experimental correlation functions were calculated by taking a time

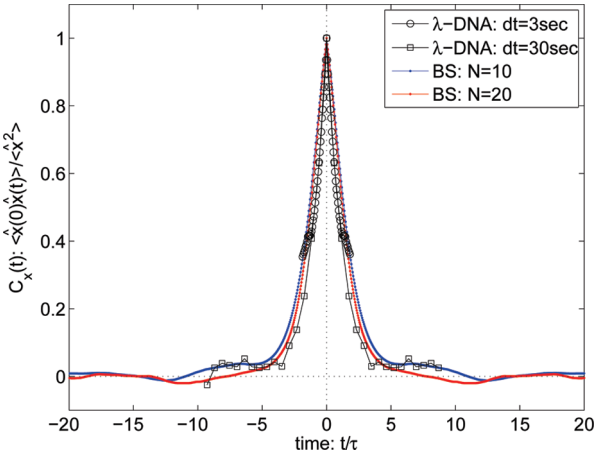

Figure 13. Extension autocorrelation at $Wi \approx 4.3 \pm 0.2$. Experimental results for 17.3 μm λ-phage DNA are in agreement with bead−spring simulations of $N_k = 153$. Extension autocorrelation decays monotonically, showing a lack of periodicity in extension.

average and a chain ensemble average over individual trajectories similar to those shown in Figure 12.

$$C_{X,Y}(t) = \frac{E[(X(s)-\mu_x)(Y(s+t)-\mu_y)]_{T,n}}{\sigma_x\sigma_y} \quad (25)$$

$$C_X(t) = \frac{E[(X(s)-\mu_x)(X(s+t)-\mu_x)]_{T,n}}{{\sigma_x}^2} \quad (26)$$

where $E[...]_{T,n}$ represent the expectation over an ensemble of times, T, and chains, n. μ_x and σ_x are defined as the average value and the standard deviation, respectively, of the stochastic variable X over the entire ensemble. The sampling time, T, was the time between frames. The stochastic variables for dilute polymer dynamics do not become uncorrelated until about 5−10 relaxation times. Although nonindependent data sets were used to create an ensemble, the ensemble sizeis taken only to be the number of independent sets.

Power spectral densities (PSD) were also calculated from correlation functions. A PSD is simply the magnitude of the Fourier transform of a correlation function. To begin, a discrete Fourier transform was performed.

$$\mathrm{DFT}[C(n)](\nu) = \sum_{n=1}^{N} C(n)\exp\left(-2\pi i\frac{(\nu-1)(n-1)}{N}\right) \quad (27)$$

where n represents an interval in time space, ν represents an interval in frequency space, and N is the total number of data points in each. Ideally, to examine 3 orders of magnitude in frequency, a single trajectory of 1000 data points is required in the temporal space correlation functions. However, because of the photobleaching limitations, two sets of data were taken in order to resolve multiple decades in Fourier space. At large time steps one is effectively truncating the frequency domain, which results in aliasing of the PSD, or a superposition of the Fourier transforms associated with higher order commensurate frequencies.[44] Assuming the PSD decays like a power law at high frequencies (which we find is correct for our simulations and experiments a posteriori), by performing experiments at small time steps, the influence of aliasing at large time steps can be quantified and eliminated.

$$\mathrm{PSD}(\nu) \approx \mathrm{DFT}[C(n)](\nu) - a\sum_{i=1}^{\infty}[(2iN-\nu)^{\beta} + (2iN+\nu)^{\beta}] \quad (28)$$

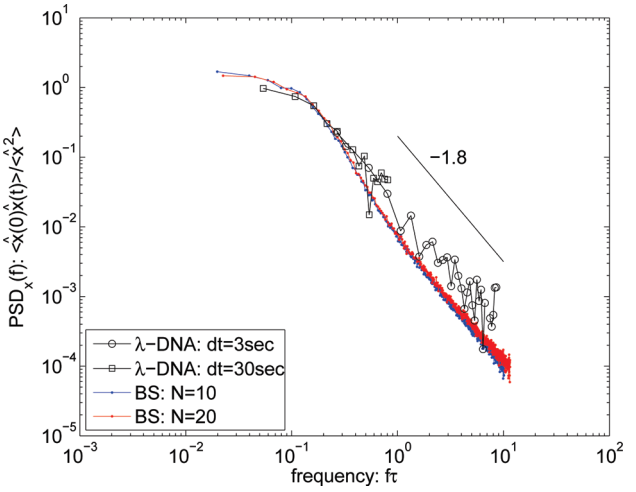

Figure 14. Extension power spectral density at $Wi \approx 4.3 \pm 0.2$.

where a and β are determined by fitting the PSD at high frequencies using a nonlinear conjugate gradient algorithm to minimize mean-square errors.

The autocorrelation function for the extension of a tethered λ-phage DNA chain and the subsequent power spectral density function are shown in Figures 13 and 14, respectively. The extension autocorrelation function proves to be a monotonically decreasing function which is nearly a simple exponential. The corresponding PSD in Figure 14 also decays monotonically with a power of −1.8.

Whereas no periodicity is seen in the autocorrelation of extension, it is found in the autocorrelation of orientation angle through the origin. Increases in height in any part of the chain will result in the chain experiencing higher drag, and thus the chain lengthens, making ϕ sensitive to cyclic motion.

The minimum in the autocorrelation represents a strong negative correlation between increases in orientation angle and a decrease following a short time later. The negative correlation is much stronger than any periodicity seen in the autocorrelation functions of height or extension, due to the fact that the orientation angle captures the connection between increases in height and a delayed increase in extension. Whereas changes in height or extension do not directly induce negative fluctuations in themselves, fluctuations in orientation angles do.

Apparent in Figure 16, the characteristic frequency of cyclic motion at $Wi = 4.3 \pm 0.2$ is 0.15 ± 0.03, made dimensionless with the relaxation time of the tethered λ-phage DNA. The characteristic frequency calculated from bead spring simulations at $Wi = 4.6$ is 0.17 ± 0.03. Perfect agreement is not expected with the effects of discretization, which increase extensional fluctuations and decrease height in the simulated chains.

The strongest evidence for the presence of cyclic dynamics lies in the cross-correlation of the height and the extension. Because a deviation in height directly causes an increase in drag and therefore, an increase in extension, there is a positive correlation between the height at $t = 0$ and the extension at $t > 0$. The cross-correlation between the height and extension is presented in Figure 17. Very strong correlation, as much as 60%, is observed for positive time at $Wi = 4.3 \pm 0.2$.

More information about the time scales of the dynamics are captured with the cross-correlation than with any autocorrelation. Positive time represents a deviation in extension at time $t > 0$ as a result of a deviation in height. Negative

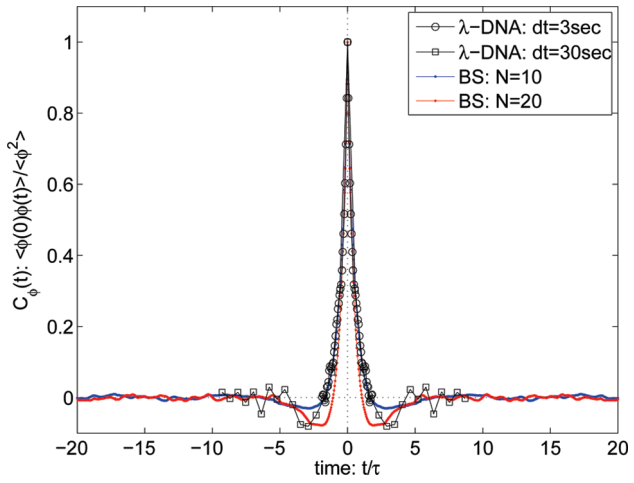

Figure 15. Autocorrelation of orientation angle through the origin at $Wi \approx 4.3 \pm 0.2$. Experimental results for 17.3 μm λ-phage DNA agree with bead−spring simulations of $N_k = 153$. Orientation angles through the origin are larger than the orientation angles through the COM and fluctuations are greater, improving the resolution of the autocorrelation function. The minimum in the autocorrelation is easily resolved experimentally and with simulations.

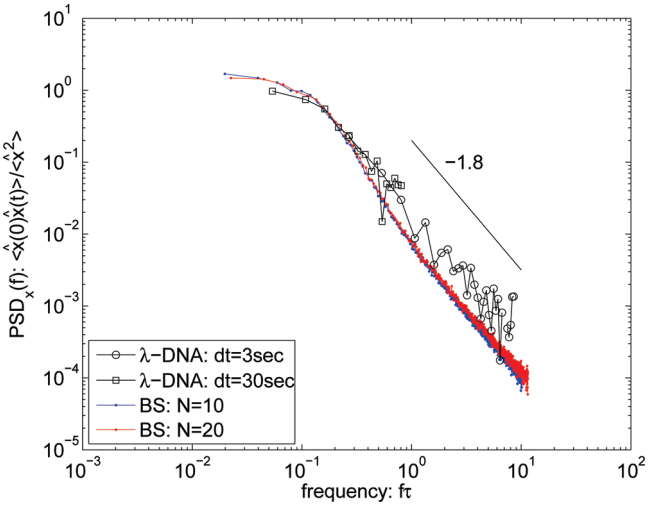

Figure 16. PSD of orientation angle through the origin at $Wi \approx 4.3 \pm 0.2$. Experimental results for 17.3 μm λ-phage DNA agree with bead−spring simulations of $N_k = 153$. A defined peak is present in each curve at $f\tau = 0.15 \pm 0.03$. This peak represents the most common frequency of the cyclic motion and proves that cyclic motion is quasiperiodic.

time represents a deviation in height at time $t > 0$ as a result of deviation in extension, as apparent by the antisymmetry of the cross-correlation function. The sign of the cross-correlation function differentiates between one variable having a positive effect on the other, such as height on extension, and one having a negative effect, such as extension on height. Figure 17 shows that for positive time there is a positive correlation that is maximized in simulations near $t/\tau = 0.54 \pm 0.02$, $C_{\delta_2} = 0.63 \pm 0.01$ and maximized in experiments near $t/\tau = 0.26 \pm 0.03$, $C_{\delta_2} = 0.56 \pm 0.01$. The time at which this maximum occurs is the most probable time it takes for a polymer to stretch out after the height of the chain increases. Simulation results also show a slight negative correlation for negative time. This effect is the result of the entropic effect at high extensions, where diffusion in the height direction is limited. This correlation is not captured from experiments due to the noise threshold. The argument that this deviation between simulation and experiments is associated with noise

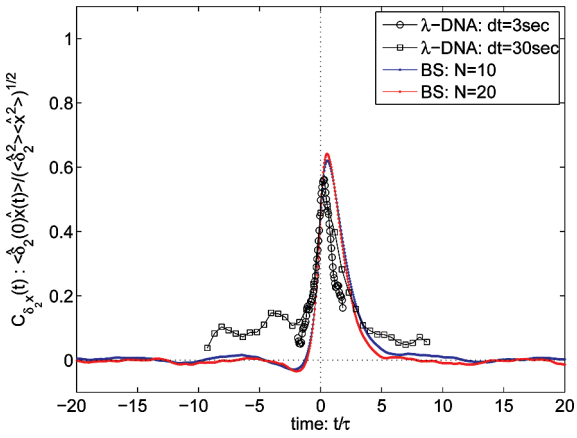

Figure 17. Cross-correlation of height and extension at $Wi \approx 4.3 \pm 0.2$. Experimental results for 17.3 μm λ-phage DNA agree with bead−spring simulations of $N_k = 153$. The presence of the trends shown in Figure 12 are quantified here. Positive time represents extension dependence on height, whereas negative time represents height dependence on extension. Both experiments and simulations reveal a maximum correlation that appears at positive time. Simulations show a negative correlation for small negative times; however, this phenomenon is unresolvable in the experimental data.

is supported by the fact that when the time step is reduced, more accurate results are obtained as shown by the open circles as compared to the open squares in Figure 17.

Not only does an increase in height have an effect on the extension, but a decrease in height does as well. If the chain diffuses closer to the wall, the extended chain will relax on the time scale of the relaxation time. The width of the peak in the cross-correlation function is a representation of this behavior. The cross-correlation function shown here is a result of the superposition of the flow-induced extension following an increase in extension and an entropic-induced relaxation following a decrease in height.

One last aspect of the cross-correlation function that provides useful information is the entire width of the peak. The sum of the time scales of restretch, recoil, and twice the entropic time scale gives the time scale for a complete cycle. Since the peaks of all the dynamics are convoluted and unresolvable, the width of the convoluted peak can be used to approximate the time scale of a complete cycle. Therefore, $t/\tau = 7.5 \pm 0.5$ provides an approximation for the average period of cyclic motion. Molecular dynamic simulations of freely jointed chains have shown this time to be 4 at $Wi \approx 4$,[15] which is in general agreement with our present results. Since, the period is inversely proportional to the frequency, we calculate $f\tau = 0.13 \pm 0.01$, which is slightly lower than the actual characteristic frequency, $f\tau = 0.15 \pm 0.03$, calculated from the orientation angle PSD.

Conclusions

Shear flow is, at least at present, the most important flow type for a tethered polymer chain in microprocessing applications. In such cases, nearly all laminar flows can be approximated as linear shear flow in close proximity to the surface (excluding stagnation point flows). Overall, the dynamics of polymer molecules are drastically affected by the presence of a wall. We demonstrated these effects using a combination of theoretical, computational, and experimental approaches.

A modification to the entropic spring force associated with free chains was made to incorporate the presence of a wall. It was found that when random walk chains are tethered to a surface, they are marked by a modification to the free space entropic forcelaw of $k_B T/y$ in the wall-normal direction. For a wormlike

chain model, the wall is more exclusive due to the requirement that the curvature of the chain is finite. For this reason, the entropic force law for a wormlike chain in the presence of a wall requires a modification of $2k_BT/y$ in the wall-normal direction. These approximations are valid for tethered chains as well as chains that are within a small distance from the wall, as compared to the radius of gyration of the chain.

Experiments in the flow gradient plane have revealed the details of cyclic dynamics for the first time. Simulations have proposed this phenomena,[13,14,45] but experiments in the flow-vorticity plane were not capable of testing it.[12,13] A maximum was found in the power spectral density functions of the polymer orientation angle, in agreement with negative oscillations in the autocorrelation function. This confirms that cyclic dynamics are quasiperiodic in nature.

Flow-gradient plane experiments also revealed that bead−spring simulations were not capable of reproducing proper values for the mean-square distance from the wall. This limitation may directly influence *Wi* scalings of the cyclic dynamics frequency predicted previously.[14] Further experimentation is required to resolve the proper scaling.

Hopefully, this work may be extended to the varied applications of tethered polymers previously discussed. For example, with the aid of the results presented here, a repeatable and controllable double tethering process could be created, enabling efficient fabrication of microelectronic devices for large-scale screening of organic semiconductors on a single molecule scale.

Acknowledgment. The authors thank the Nanoscale Interdisciplinary Research Team, a National Science Foundation funded organization, for financially supporting this work under Grant DMR-0507296.

References and Notes

(1) Klein, J. *Proc. Inst. Mech. Eng., Part J* **2006**, *220*, 691–710.
(2) Klein, J.; Perahia, D.; Warburg, S. *Nature* **1991**, *352*, 143–145.
(3) Klein, J.; Kumacheva, E.; Mahalu, D.; Perahia, D.; Fetters, L. *Nature* **1994**, *370*, 634–636.
(4) Zammatteo, N.; Jeanmart, L.; Hamels, S.; Courtois, S.; Louette, P.; Hevesi, L.; Remacle, J. *Anal. Biochem.* **2000**, *280*, 143–150.
(5) Oh, S.; Cho, S.; Kim, C.; Park, J. *Biol.* **1997**, *119*, 189–201.
(6) Elbert, D.; Hubbell, J. *Annu. Rev. Mater. Sci.* **1996**, *26*, 365.
(7) Moro, T.; Takatori, Y.; Ishihara, K.; Konno, T.; Takigawa, Y.; Matsushita, T.; Chung, U.; Nakamura, K.; Kawaguchi, H. *Nat. Mater.* **2004**, *3*, 829–836.
(8) Blainey, P.; van Oijen, A.; Banerjee, A.; Verdine, G.; Xie, X. *Proc. Natl. Acad. Sci. U.S.A.* **2006**, *103*, 5752–5757.
(9) Braun, E.; Eichen, Y.; Sivan, U.; Ben-Yoseph, G. *Nature* **1998**, *391*, 775.
(10) Lee, J.; Jung, Y.; Stoltenberg, R.; Tok, J.; Bao, Z. *J. Am. Chem. Soc.* **2008**, *130*, 12854–12855.
(11) Lee, J. K.; Jaeckel, F.; Moerner, W. E.; Bao, Z., in press, **2009**.
(12) Ladoux, B.; Doyle, P. S. *Europhys. Lett.* **2000**, *52*, 511.
(13) Doyle, P. S.; Ladoux, B.; Viovy, J. L. *Phys. Rev. Lett.* **2000**, *84*, 4769.
(14) Schroeder, C. M.; Teixeira, R. E.; Shaqfeh, E. S. G.; Chu, S. *Phys. Rev. Lett.* **2005**, *95*, 018301.
(15) Delgado-Buscalioni, R. *Phys. Rev. Lett.* **2006**, *96*, 88303.
(16) Kratky, O.; Porod, G. *Recl. Trav. Chim.* **1949**, *68*, 1106.
(17) Juan, W.-T.; Chu, S., in preparation, **2009**.
(18) Juan, W.-T.; Chu, S., to be submitted, **2009**.
(19) Teixeira, R. E. Ph.D. Thesis, Stanford University, **2005**.
(20) Rodney, W.; Spindler, R. *J. Opt. Soc. Am.* **1954**, *44*, 677–679.
(21) Properties of Fused Quartz; Technical Glass Products, Inc., 2000−2008, Retrieved Jan 8, 2008, http://www.technicalglass.com/tech.htm.
(22) Lide, D. *CRC Handbook of Chemistry and Physics: A Ready-Reference Book of Chemical and Physical Data*; CRC Press: Boca Raton, FL, 2004.
(23) Savage, M.; Co, P. *Avidin-Biotin Chemistry: A Handbook*; Pierce Chemical Co.: Rockford, IL, 1992.
(24) Weber, P.; Ohlendorf, D.; Wendoloski, J.; Salemme, F. *Science* **1989**, *243*, 85.
(25) Hendrickson, W.; Pahler, A.; Smith, J.; Satow, Y.; Merritt, E.; Phizackerley, R. *Proc. Natl. Acad. Sci. U.S.A.* **1989**, *86*, 2190–2194.
(26) Du, Q.; Smith, C.; Shiffeldrim, N.; Vologodskaia, M.; Vologodskii, A. *Proc. Natl. Acad. Sci. U.S.A.* **2005**, *102*, 5397–5402.
(27) Kramers, H. A. *Collected Scientific Papers*; North-Holland Publishing Co.: Amsterdam, 1956.
(28) Somasi, M.; Khomami, B.; Woo, N. J.; Hur, J. S.; Shaqfeh, E. S. G. *J. Non-Newtonian Fluid Mech.* **2002**, *108*, 227.
(29) Marko, J. F.; Siggia, E. D. *Macromolecules* **1995**, *28*, 8759.
(30) Öttinger, H. C. *Stochastic Processes in Polymer Fluids*; Springer: Berlin, 1996.
(31) Liu, T. W. *J. Chem. Phys.* **1989**, *90*, 5826.
(32) Beck, V. A.; Shaqfeh, E. S. G. *J. Chem. Phys.* **2006**, *124*, 094902.
(33) Jendrejack, R. M.; Schwartz, D. C.; de Pablo, J. J.; Graham, M. D. *J. Chem. Phys.* **2004**, *120*, 2513.
(34) Yamakawa, H. *Modern Theory of Polymer Solutions*; Harper & Row: New York, 1971.
(35) Evans, A. R. Ph.D. Thesis, Stanford University, **1995**.
(36) Ermak, D. L.; McCammon, J. A. *J. Chem. Phys.* **1978**, *69*, 1352.
(37) Hsieh, C. C.; Li, L.; Larson, R. G. *J. Non-Newtonian Fluid Mech.* **2003**, *113*, 147.
(38) Bustamante, C.; Marko, J. F.; Siggia, E. D.; Smith, S. *Science* **1994**, *265*, 1599.
(39) Woo, N.; Shaqfeh, E.; Khomami, B. *J. Rheol.* **2004**, *48*, 281.
(40) Lehner, R.; Koota, J.; Maret, G.; Gisler, T. *Phys. Rev. Lett.* **2006**, *96*, 107801.
(41) Schroeder, C.; Babcock, H.; Shaqfeh, E.; Chu, S. *Science* **2003**, *301*, 1515–1519.
(42) Perkins, T.; Smith, D.; Chu, S. *Science* **1994**, *264*, 822–826.
(43) Weisstein, E. W. Cross Correltation Theorem; **2009**, Retrieved Jan 29, 2009, http://mathworld.wolfram.com/Cross-CorrelationTheorem.html.
(44) Bracewell, R. N. *The Fourier Transform and Its Applications*; McGraw-Hill Co.: New York, 2000.
(45) Doyle, P.; Shaqfeh, E.; Gast, A. *J. Fluid Mech.* **1998**, *31*, 5474–5486.